“Influence of embedded $MoSi_2$ particles on the high temperature thermal conductivity of SPS produced yttria-stabilised zirconia model thermal barrier coatings”

Justyna Kulczyk-Malecka[a]*, Xun Zhang[a], James Carr[a], Alexandra L. Carabat[b], Willem G. Sloof[b], Sybrand van der Zwaag[c], Federico Cernuschi[d], Franck Nozahic[e], Daniel Monceau[e], Claude Estournès[f], Philip J. Withers[a], Ping Xiao[a]

[a] School of Materials, The University of Manchester, M13 9PL, UK

[b] Department of Materials Science and Engineering, Delft University of Technology, Mekelweg 2, 2628 CD Delft, The Netherlands

[c] Faculty of Aerospace Engineering, Delft University of Technology, Kluyverweg 1, 2629 HS Delft, The Netherlands

[d] RSE S.p.a., Via Rubattino, 54, 20134 Milano (MI), Italy

[e] CRIMAT, Université de Toulouse, CNRS, INPT, UPS, ENSIACET, 4 allée Emile Monso BP-44362, 31030 Toulouse Cedex 4, France

[f] CIRIMAT, Université de Toulouse, CNRS, INPT, UPS, 118 Route de Narbonne, F-31062 Toulouse, France

Abstract:

To prolong the lifetime of thermal barrier coatings (TBCs) recently a new method of microcrack healing has been developed, which relies on damage initiated thermal decomposition of embedded molybdenum disilicide ($MoSi_2$) particles within the TBC matrix. While these $MoSi_2$ particles have a beneficial effect on the structural stability of the TBC, the high thermal conductivity of $MoSi_2$ may have an unfavourable but as yet unquantified impact on the thermal conductivity of the TBCs.

In this work the thermal conductivity of spark plasma sintering (SPS) produced yttria-stabilised zirconia (YSZ) model thermal barrier coatings containing 10 or 20 volume percent of $MoSi_2$ healing particles was investigated using the laser flash method. Measurements were performed on free-standing composite material over a temperature range from room temperature up to 1000 °C. Microstructural analysis was carried out by SEM combined with image analysis to determine the size, distribution and area fraction of healing particles. The measurements were compared with the results from microstructure-based multi-physics finite element (FE) models and analytical models (the asymmetric Bruggeman model and the Nielsen model) in order to study the effects of the addition of $MoSi_2$ particles as well as the presence of micro-pores on the apparent thermal conductivity. The results show a strongly non-linear increase in the thermal conductivity of the composite material with the $MoSi_2$ volume fraction and a dependence on the aspect ratio of $MoSi_2$ particles. Interparticle connectivity is shown to play a big role too.

Key words:

Thermal conductivity, Thermal barrier coatings, Self-healing materials, Spark plasma sintering.

*Corresponding author: justyna.kulczyk-malecka@manchester.ac.uk
Tel: +441613063590

1. Introduction

Yttria-stabilised zirconia (YSZ) has one of the lowest thermal conductivity values among ceramic materials, and therefore is widely used as the base material in thermally protective coatings for gas turbines components in aircraft engines and power generators. These thermal barrier coatings (TBCs) are generally deposited onto the metallic components by atmospheric plasma spraying (APS) or electron beam physical vapour deposition (EB-PVD) methods. The coated systems experience high stresses that develop due to the thermal expansion coefficients mismatch between the metal substrate and the ceramic TBC. Upon a sufficient number of cycles these stresses may result in the development of microcrack patterns in the TBC that coalesce and ultimately lead to failure of the topcoat and its adhesion promoting thermally grown oxide (TGO) layer [1-4]. For TBC systems manufactured by APS failure is known to occur within the porous YSZ top coat close to the TGO layer [3]. Therefore, it has been proposed to embed 'healing' particles inside the YSZ top coat, which when intersected by a crack initiate a chemical reaction resulting in filling the microcracks with a well-adhering load bearing substance [5-7]. The healing action makes that the crack effectively disappears, restores the TBC mechanical integrity and extends the life time of the component [5]. It has been demonstrated that B-containing molybdenum disilicide ($MoSi_2$) could act as a suitable healing agent for YSZ-based TBCs. Upon oxidation initially silica (SiO_2) is formed as a reaction product, which fills the crack and subsequently turns into mechanically stable zircon ($ZrSiO_4$) due to a secondary solid state chemical reaction with the YSZ matrix [7, 8]. To prevent premature oxidation of the $MoSi_2$ in the absence of a crack, the $MoSi_2$ particles need to be protected by a very thin yet dense layer of alumina [8], such that the self-heling mechanism would only be initiated by a crack intersecting the particle and opening the shell, allowing $MoSi_2$ oxidation.

The presence of such $MoSi_2$ particles could have other (negative) effects on other important properties, such as the thermal conductivity value, of the TBC too. It has been shown that

*Corresponding author: justyna.kulczyk-malecka@manchester.ac.uk
Tel: +441613063590

doping of YSZ with sub-tetravalent oxides could further reduce thermal conductivity of YSZ as it leads to the formation of oxygen vacancies that strongly scatter phonons [9-11]. However, embedding $MoSi_2$ particles in a regular YSZ does not promote the formation of oxygen vacancies and $MoSi_2$ itself, being a intermetallic compound, shows a high thermal and electrical conductivity instead [12, 13]. Since the thermal conductivity of $MoSi_2$ is much higher than that of YSZ [12] and the TBC system as a whole [14, 15] it is important to investigate the unwanted decrease in thermal insulation due to the embedment of $MoSi_2$ particles. Therefore, in this paper the potentially negative effect of embedded $MoSi_2$ particles on the global thermal conductivity of the composite YSZ material has been investigated as a function of the $MoSi_2$ particle fraction and morphology, both experimentally and theoretically. It should be pointed out that in the case of successful implementation of such healing particles in TBCs they are expected to remain intact for a very long time and only to be activated towards the end of the life time of the coating. Hence, it is important to study the reduction of the thermal insulation of the underlying turbine blade for intact particles. As the final reaction product, after the occurrence of the healing reaction ($ZrSiO_4$), is a non-conducting material, the healing reaction itself will only be beneficial for the thermal protection itself.

Since APS deposition of YSZ thermal barrier coatings containing controlled amounts of $MoSi_2$ particles of specified shape and integrity is technologically very complex and part of ongoing international research, in the present work we focus on free standing YSZ material containing different volume percentages of $MoSi_2$ particles manufactured by a spark plasma sintering (SPS) method. The homogenous distribution of the $MoSi_2$ particles in the YSZ sample created and analysed here provides an upper boundary for the actual loss in thermal protection for the envisaged TBC systems, which will only contain $MoSi_2$ particles close to the interface with the TGO, as this is the region in which the lateral cracking is found to occur [3]. Certainly there is no need to insert $MoSi_2$ particles in regions of the TBC where cracking does not lead to spallation of TBC. Localised deposition of the $MoSi_2$ particles at well-defined positions in the

TBC can be achieved by dual particle feed APS processing and taking appropriate measures to compensate for the partial decomposition of the $MoSi_2$ particles during spraying. The SPS process taking a process cycle of typically one hour is a more benign production process than the APS process with its supersonic acceleration of the particles through the plasma and a process time well within a second. Therefore SPS is a suitable technique to produce model TBC systems for studies as reported here. It should be pointed out that SPS produced YSZ material is less porous than a typical APS TBCs. However the effect of porosity, pore shapes and its extension on the thermal conductivity of YSZ have been studied previously [15-17] and can be compensated for in the present experimental work. The aim of this work is to quantitatively investigate the influence of embedding $MoSi_2$ particles on the thermal insulating performances of YSZ. In companion work the effect of the concentration and aspect ratio of the healing particles on the crack healing action is being studied [18]. Ultimately one can define the optimal combination of improvement in thermomechanical stability, resulting extension of the life time and reduction in thermal protection of the underlying turbine blades as a function of the $MoSi_2$ concentration and particle morphology, and work of this nature forms the core target of the EU funded SAMBA project [19] and the final results will be reported in due course.

2. Experimental

Disc shaped YSZ samples with embedded $MoSi_2$ particles were prepared by SPS. The powder mixtures were produced by mixing yttria-stabilized zirconia containing 7 wt. % Y_2O_3 (YSZ Amperit 872, H.C. Starck, average particle size of 7 µm) and molybdenum silicide ($MoSi_2$, 99.5 % purity, ChemPur GmbH, average particle size of 5 µm) using a CAT RM5W-80V roller mixer. The mixing was carried out for 12 h. The volume fraction of $MoSi_2$ particles was varied between 10 and 20 vol. %. Prior to sintering, the YSZ powder was downsized from 40 µm to 7 µm using a Retsch PM 100 planetary ball milling. Zirconia balls of 10 mm diameter were used as grinding media. The ball to powder mass ratio was kept to 3:1. The rotor speed was 300 rpm and the milling time was 24 h.

The particle size distribution of YSZ and $MoSi_2$ particles was determined using a Malvern Master Sizer X laser diffraction instrument (Malvern Instruments Ltd., Worcestershire, UK). Prior to the measurements, the particles were ultrasonicated in water for 20 min.

A 20 mm inner diameter graphite die was employed to sinter the composites in the SPS installation (FCT SPS system, type KCE-FCT HP D-25-SI, Germany). To prevent any possible reaction between the graphite die and the powders, a graphitic paper was placed between the punches and the powder as well as between the die and the powder. The graphitic paper was sprayed with BN on the both sides for easy removal. The powders were sintered in vacuum at 1500 °C with a heating rate of 20 °C/min and an isothermal hold of 30 min under a constant uni-axial pressure of 50 MPa applied since the beginning of the sintering cycle. The temperature was monitored using an axial pyrometer. The electric current was applied by pulse following the standard 15/5 (on/off 3 ms) pulse pattern. Natural cooling was applied from the sintering temperature to room temperature, after releasing the pressure. The sintering results in disc like samples of 20 mm diameter and about 2 mm thickness.

The microstructure of the samples was investigated by scanning electron microscopy (FEG-SEM, Quanta 650) using backscatter electron (BSE) detector. Specimens were subjected to X-ray diffraction (XRD) (Philips X'Pert), from which the phase composition was obtained. The bulk densities of the samples were measured by the Archimedes method according to ASTM 13962 standard test method for density of compacted or sintered powder, whereas the volume fraction and the geometrical characteristics of the porosity was evaluated by computerised image analysis using Avizo software.

The thermal diffusivity of the samples was measured from room temperature up to 1000 ^{o}C in an argon atmosphere using an in-house constructed laser flash system. Prior to analysis samples were machined to discs of approximately 10 mm diameter and approximately 2 mm thickness. Both surfaces of the specimen were coated with a thin layer of colloidal graphite to enable uniform energy absorption of the laser pulse. During the measurements the entire front face of the sample was exposed quasi homogeneously to a short duration heat pulse (0.67 ms), which was supplied by a neodymium glass laser. An InSb infrared detector, cooled in liquid nitrogen, was used to measure the temperature rise on the reverse side of the samples. Measurements were made at various temperatures during the heating up procedure at approximately 100 ^oC intervals. For each temperature at least 7 measurements were taken to obtain mean accurate thermal diffusivity values.

The thermal conductivity values were obtained from the bulk density (ρ), specific heat (C_p) and thermal diffusivity (α) using the following relationship:

$$k = \rho \cdot C_p \cdot \alpha \qquad (1)$$

The specific heat capacity values were calculated accordingly to the Neumann-Kopp rule [20] based on referenced specific heat values reported in Barin [21] and calculated for the corresponding molar fractions of $MoSi_2$ particles within the YSZ matrix.

2.1 The analytical models for thermal conduction in composite materials

Bruggeman model has been widely applied to estimate thermal conductivity values of two-phase systems as a function of the volume fraction of the dispersed phase and the properties of the constituent phases [22-24]. The model has also been used in this work to predict *k* values for the composite materials synthesized.

Based on the asymmetric Bruggeman model, the effective thermal conductivity of an inter-connected two phase composite is related to the composition according to [23, 25]:

$$(1-f) = \left(\frac{k_m}{k_{eff}}\right)^{\zeta} \frac{k_d - k_{eff}}{k_d - k_m} \left(\frac{k_{eff} + \gamma k_d}{k_m + \gamma k_d}\right)^{\eta} \qquad (2)$$

where k_{eff} is the effective thermal conductivity of a two-phase asymmetric system containing a volumetric fraction f of dispersed spheroids; k_d is the thermal conductivity of dispersed spheroids; k_m is the thermal conductivity of the continuous matrix and ζ, γ and η are related to the relative orientation between thermal flux and the shape of dispersed particles [26]. The shapes of the spheroids can vary from a cylinder up to a flat lamella and can be suitably described by the axial ratio *a:c* of the spheroids [27].

Another analytical model for the thermal conductivity of two-phase system that has been applied in this work is that by Nielsen [28, 29]. The Nielsen model is an empirical model with adjustable fitting parameters that has been widely used to predict thermal conductivity of the two-phase system consisting of a matrix and a filler having significantly different thermal properties [22, 23, 30, 31]. The analytical solution can be found from the following formulae:

$$\frac{k}{k_1} = \frac{1+AB\varphi_2}{1-B\psi\varphi_2} \tag{3}$$

$$A = k_E - 1 \tag{4}$$

$$B = \frac{k_2/k_1-1}{k_2/k_1+A} \tag{5}$$

$$\psi \cong 1 + \left(\frac{1-\phi_m}{\phi_m^2}\right)\varphi_2 \tag{6}$$

where k_1 and k_2 represent thermal conductivities of the matrix and the filler, respectively; k_E is generalised Einstein coefficient; constant A depends on the shape of the dispersed particles and their orientation in respect to the heat flux; constant B accounts for the relative thermal conductivity of the two components; φ_2 is the volume fraction of dispersed phase; and ψ is determined by the maximum packaging fraction φ_m. The φ_m is defined as the true volume of the particles divided by the volume they appear to occupy when packed to their maximum extent [28].

3. An actual microstructure-based 2D FE model for thermal conduction

To quantitatively correlate the microstructural features to the effective thermal conductivity of the samples, we developed an image-based 2D multi-physics finite element (FE) model to calculate the effective thermal conductivity for composites having exactly the microstructure as derived from SEM images. The SEM images were first filtered to remove any noise that may come from image acquisition process. Afterwards, the filtered image (Fig. 1 a) was segmented based on both the grey value of each pixel and the topological feature of the particles. A top-hat method for segmentation from Avizo software was employed to separate pores, $MoSi_2$ particles and YSZ matrix. Each phase in the SEM image was labelled and assigned a typical

*Corresponding author: justyna.kulczyk-malecka@manchester.ac.uk
Tel: +441613063590

value (Fig. 1 b). 2D FE meshes were generated using the segmented images with ScanIP® software. Each SEM image comprised of 1024 × 884 pixels. The mesh densities at the YSZ/$MoSi_2$ and solids/pores interfaces were refined for computation accuracy. As the thermal conductivity of gas (~ 0.024 $Wm^{-1}K^{-1}$ and decreasing dramatically as temperature increases) is much lower than that of the YSZ (~ 2 $Wm^{-1}K^{-1}$ at room temperature), we assumed that pores act as thermal insulators in the model [32]. Therefore, no meshes have been generated within the pores. The final FE mesh consisted of 3000000 ~ 4000000 DC2D3 elements (Fig. 1 c) and a constant heat flux was applied along the global X-axis. The effective thermal conductivity of the ceramic composite was calculated based on the temperature at two edges of the sample (Fig. 1 d) when a steady state is reached according to:

$$k_{eff} = \frac{q \times L}{\Delta T} \tag{7}$$

where L is the dimension of the SEM image in the direction of the heat flux, q is the integrated heat flux intensity and ΔT is calculated as the average temperature difference at two edges perpendicular to the heat flux direction.

The conductivity of YSZ is assumed to be more or less independent of the temperature as has been reported previously [17]. This property of YSZ has been ascribed to the high defect density. At 100 °C the thermal conductivity value for YSZ is 2 $Wm^{-1}K^{-1}$ [15]. On the other hand, the thermal conductivity of $MoSi_2$ is highly temperature sensitive in comparison to YSZ. Fig. 2 shows this temperature dependence [12].

4. Results

4.1 Microstructure and phase identification

Fig. 3 shows BSE-SEM images of the composite materials. The pores can be easily distinguished as the dark phase. Healing particles are the grey phase, while YSZ is the brightest phase. Avizo software was used to segment out such pores based on a global grey value threshold and quantify their volume percentage and morphology. Microstructural details for the three composite grades are listed in Table 1.

As-received samples were also characterised using XRD analysis under Cu Kα radiation. Samples were scanned from 20.01 to 84.99 2θ degrees with 0.02 step size. Fig. 4 shows XRD data obtained from the samples. It can be seen that besides YSZ and $MoSi_2$ some traces of Mo_5Si_3 are present in the sample with 10 vol. % of healing particles., Mo_5Si_3 has been reported to have a lower thermal and electrical conductivity than $MoSi_2$ [33, 34]. However, as the amount of Mo_5Si_3 in the composite is minimal, we have neglected its effect on the sample's effective thermal conductivity.

4.2 Thermal conductivity

Fig. 5 shows the thermal diffusivity of the three composites as a function of the temperature. From a temperature of 100 ^{o}C for all three compositions the thermal diffusivity decreases continuously with increasing temperature. The largest drop in thermal conductivity with temperature occurs in the sample containing 20 vol. % of $MoSi_2$. As expected, the impact of embedding $MoSi_2$ in YSZ on its thermal diffusivity is manifested in two ways: (1) the thermal diffusivity values doubles from the value for pure YSZ sample to the one doped with 20 vol. % of $MoSi_2$ and (2) the thermal diffusivity of the composite becomes more temperature dependent as the $MoSi_2$ volume fraction increases (see also Fig. 2).

Fig. 6 shows the calculated thermal conductivity values of the three samples as a function of the temperature (Eq. 1). The figure shows that the thermal conductivity value for the un-doped YSZ is almost temperature independent. This phenomenon is characteristic for pure YSZ and agrees with the literature [15, 17, 35]. However, in composite samples the thermal conductivities show significantly higher values and a clear temperature-dependent curvature is visible for the sample containing 20 vol. % $MoSi_2$. This is due to the $MoSi_2$ dopant, which is known to have a good thermal (and electrical) conductivity, reported to be about 68 $Wm^{-1}K^{-1}$ at room temperature [12] dropping to about 30 $Wm^{-1}K^{-1}$ at 1000 ^{o}C (Fig. 2).

4.3 Effective thermal conductivity from the analytical and numerical models

*Corresponding author: justyna.kulczyk-malecka@manchester.ac.uk
Tel: +441613063590

The thermal conductivity values as obtained by the laser flash method and as calculated using the Bruggeman model and the image-based FE model are plotted in Fig. 7 a and b as a function of temperature for composites containing 10 and 20 vol. % of $MoSi_2$, respectively. The dashed lines represent lower and upper bounds that have been calculated from asymmetric Bruggeman model that assumes that the secondary phase is dispersed within a continuous matrix. In the lower estimate the model presumes that the less-conductive (i.e. YSZ) phase is the continuous phase and the more-conductive (i.e. $MoSi_2$) phase is dispersed. In the upper estimate the assumptions are inversed. Fig. 7 a shows that in the case of the 10 vol. % $MoSi_2$ composite the symmetric Bruggeman estimate, the lower bound Bruggeman value and the FEM value are rather close and a little lower than the experimental value, yet all data sets showing the same temperature dependence. All values are considerable lower than the upper bound estimate, as is to be expected given the dispersed nature of the $MoSi_2$ particles observed in SEM. In the case of the 20 vol. % $MoSi_2$ composites again the symmetric Bruggeman estimate, the lower-bound Bruggeman value and the FEM value are rather close. In this case the experimental data are much higher than predicted, but more interestingly retain their predicted weak temperature dependence.

The Nielsen model (Eq. 3-6) predictions and experimental effective thermal conductivity values at room temperature are plotted as a function of the actual volume fraction of $MoSi_2$ in Fig. 8. The best fit was obtained for a shape factor A=2.72 and a maximum packaging fraction $\varphi_{m,}$=0.38. Using these room temperature fitting values, the Nielsen model predicts thermal conductivity values close to those obtained experimentally for the whole temperature range explored (Fig. 9).

5. Discussion

Embedding $MoSi_2$, which is a good thermal conductor, in an YSZ matrix which is an excellent insulator, can be expected to lead to an increased thermal conductivity of the composite in comparison with pure YSZ. Indeed, the experimental results have shown an obvious increase in measured thermal conductivity for the composites (Fig. 5-9). However, the measured values are higher than the predictions from asymmetric Bruggeman model for two-phase system and the FE model (Fig. 7). This discrepancy is more obvious in composites with higher content of the $MoSi_2$. To explain the mechanisms through which the addition of $MoSi_2$ particles has boosted the effective thermal conductivity, we investigated factors including conductivity, shape, orientation and percolation of the second-phase particle. FE models were used in this work as a main tool in parametric study on the effect of material’s microstructure on thermal conductivity. We focus on microstructural features that create local delocalised heat channels or channel segments through the matrix.

5.1 Effect of the porosity

The effect of porosity on the effective thermal conductivity of ceramics has been investigated extensively [15, 27, 36] and pores are supposed to be thermally non-conductive. Actually, thermal conductivity $k_{enclosed}$ of enclosed gas is described by Knudsen as [37]:

$$k_{enlosed} = \frac{k_{free}}{1+C\left(\frac{T}{P\delta}\right)} \tag{8}$$

where C is related to the gas properties.

A plot was made using the data for Ar [38] as shown in Fig. 10. SEM images in Fig. 3 indicates that the diameter of the pores lay more or less within $10^{-7} \sim 10^{-6}$ m. This corresponds to a normalised thermal conductivity of 0.2 ~ 0.8 depending on temperature. As shown in Fig. 3 the pores in the SPS produced samples seem isolated and there are no indications of longer channels in the 20 vol. % material than for the other materials. This, in combination with the 20 vol. % sample having a comparable porosity density as the 0 vol. % sample, suggest that pore connectivity is a likely explanation for the observed higher conductivity of the 20 vol. % sample.

5.2 Effects related to particle shape and orientation

Apart from the volume percentage of the second-phase material higher order parameters, such as particle size, shape and spatial distribution, can also affect the effective conductivity [15,

*Corresponding author: justyna.kulczyk-malecka@manchester.ac.uk
Tel: +441613063590

17]. To investigate the shape and orientation effect, we constructed certain artificial microstructures derived from the SEM determined real microstructure for the 20 vol. % sample. Artificial microstructures were constructed using an in-house code adapted from a circle-filling algorithm changing the *a:c* ratios by elongating the particles in directions parallel to the heat flux (*a:c* increases) and perpendicular to the heat flux (*a:c* is reduced). Please note that in all simulations the $MoSi_2$ particles remain isolated from each other. Pores and their size distributions are identical for all cases. The effective thermal conductivities have been calculated for each artificial microstructure and they have been plotted as a function of aspect ratio *a:c* in Fig. 11.

Fig. 12 shows the calculated heat flux map for four typical microstructures. It is important to note that $MoSi_2$ particles elongated along the temperature gradient direction serve as preferred pathways for heat flux due to enhanced thermal conductivity. Such pathways account for the dramatic increase in effective thermal conductivity when the *a:c* value is increased (Fig. 7). Nevertheless, it is important to stress here that the extreme orientations of the particles considered here (for the *a:c* ratios above 1:8 and 8:1) cannot be achieved by the SPS (or any of the other known) manufacturing process. Therefore, the extremes examined here only have a purely theoretical relevance and to explore the boundaries of the potential influence of the particle shape and orientation on the nett thermal conductivity of the two-phase system.

As it can be seen, the shape and orientation of $MoSi_2$ particles can have a significant effect on the effective thermal conductivity. Nevertheless, this still could not explain the higher values from experimental measurements compared with model predictions. In fact, having irregular shapes, the $MoSi_2$ particles are not preferentially oriented (see Fig. 1 a, for example). Hence $MoSi_2$ particle shape alone cannot explain the non-linear increase in thermal conduction with increasing $MoSi_2$ concentration.

5.3 Percolation effects

Percolation is the phenomenon of a rapid rise in electrical or thermal conductivity at certain concentration due to the unintentional formation of chains of more-or-less connecting particles spanning the complete distance between the two external surfaces at different temperatures of voltages. The critical percentage of filler particles at which such a chain statistically forms is called the percolation threshold. Therefore, bond percolation is used to explain the formation of conductive networks by the dopant in ceramic composite material [39, 40] as well as carbon fibre reinforced composites [41-45].

As can be seen from Fig. 7 the Bruggeman based on idealised spherical or ellipsoidal particles and FE models based on 2D representations of the actual microstructure give similar results suggesting that the particle morphology as such has not lead to the discrepancy and the FE model has captured the morphological effects of the secondary phase particles. The FE and Bruggeman model predictions only fit the data for a composite sample with 10 vol. % of $MoSi_2$. In the 20 vol. % sample the experimental values are significantly higher than these predicted from the models. This could be related to local (out of plane) interconnection of $MoSi_2$ particles in 3D that creates a fast channel for heat to transfer across the sample volume. This way heat would be transferred through the highly conductive particles embedded into less-conductive YSZ matrix resulting in significant increase of the thermal conductivity of the composite material.

However, experimental values lay within the boundary region predicted from asymmetric Bruggeman model plotted in Fig. 7 as dashed lines. It can be seen that in case of sample with 10 vol. % of $MoSi_2$ experimental values are close to the lower boundary region, whereas in sample embedded with higher fraction of $MoSi_2$ experimental values are in the range of the higher boundary limit. This could suggest that the sample with 20 vol. % of embedded particles has reached the percolation threshold, therefore does not follow Bruggeman's nor 2D SEM image-based FE model.

Experimental values fitted to the numerical Nielsen model with the factor A=2.72 and the maximum packaging fraction, $\varphi_{m,}$=0.38 gives a satisfactory fit over the whole temperature range investigated in this study (see Fig. 9). It is worth mentioning here that factor A proposed by Nielsen for spheres is 1.5, however it has been observed that for irregular, agglomerated fillers the fit factor A generally has a value higher than 2 [28]. Moreover, the maximum packaging fraction of 0.38 does not correspond to any type of packaging of spheres proposed by Nielsen. However, Pal compared the Nielsen numerical fit to various composite systems and concluded that the values of φ_m are dependent on the system that is being considered and can vary for 0.32-1.0 without any obvious explanation [46]. Maximum packaging fraction can vary between different systems due to variations in the particle size distribution and particle shape, and due to possible aggregation of filler particles. Also Weber *et al.* [47] explored the rigour of the fitting of both parameters A and φ_m and concluded that the A factor gives the greater opportunity for optimisation. It is worth stressing again that Nielsen model is an empirical model with adjustable fitting parameters and for unknown systems one cannot predict the volume dependence.

6. Conclusions

The experimental and computational work on SPS produced YSZ-$MoSi_2$ granulate composites have shown that indeed the thermal conductivity increases and becomes more temperature dependent, in accordance with the properties of the $MoSi_2$ particle. At low volume fraction of 10 vol. % the results are in reasonable agreement with the Bruggeman model and 2D FE model calculations. At the higher volume fraction of 20 vol. % the increase in thermal conduction is much stronger than predicted by the Bruggeman and FE models, which basically see the particles as fully isolated spheres in a continuous matrix. The volume fraction dependence is well described by the Nielsen model when assuming a non-spherical shape (A=2.72) and a low potential packing behaviour (φ_m = 0.38).

The current research suggested that $MoSi_2$ healing particles can be added to YSZ based thermal barrier coatings up to a volumetric concentration of 10 % without an unacceptable loss in effective thermal insulation behaviour. In case such coatings were to be produced via APS the natural splat morphology would lead to a favourable particle aspect ratio making it possible to raise the critical concentration beyond the current estimate of 10 vol. %.

The work showed that 2D based physical transport models accurately copying actual micrographs can give misleading results even for modest filling fractions of the conductive phase due to out-of-plane interconnects between particles. 3D modelling in combination with 3D imaging seems the obvious next step forward.

Acknowledgments

This project has received funding from European Union Seventh Framework Programme (FP7/2007-2013) under grant agreement no 309849, SAMBA (website: www.sambaproject.eu).

*Corresponding author: justyna.kulczyk-malecka@manchester.ac.uk
Tel: +441613063590

References:

1. Evans, A.G., Clarke, D. R., Levi, C. G., *The influence of oxides on the performance of advanced gas turbines.* J. Eur. Ceram. Soc., 2008. **28**: p. 1405–1419.

2. Heeg, B., Tolpygo, V. K., Clarke, D. R., *Damage Evolution in Thermal Barrier Coatings with Thermal Cycling.* J. Am. Ceram. Soc., 2011. **94**: p. S112–S119.

3. Schlichting, K.W., Padture, N. P., Jordan, E. H., Gell, M., *Failure modes in plasma-sprayed thermal barrier coatings.* Materials Science and Engineering A, 2003. **342**: p. 120-130.

4. Vassen, R., Jarligo, M. O., Steinke, T., Mack, D. M., Stiver, D., *Overview on advanced thermal barrier coatings.* Surface and Coating Technology, 2010. **205**: p. 938-942.

5. Sloof, W.G., *Self Healing in Coatings at High Temperature in Self Healing Materials*, in *Self Healing Materials*, S. van der Zwaag, Editor. 2007, Springer: The Netherlands. p. 309-321.

6. Sloof, W.G., Turteltaub, S. R., Carabat, A. L., Derelioglu, Z., Ponnusami, S. A., Song, G. M. , *Crack healing in yttria stabilized zirconia thermal barrier coatings*, in *Self healing materials – Pioneering research in the Netherlands*, S. van der Zwaag, Brinkman, E., Editor. 2016, IOS Press: The Netherlands. p. 219-227.

7. Derelioglu, Z., Carabat, A. L., Song, G. M., van der Zwaag, S., Sloof, W. G., *On the use of B-alloyed $MoSi_2$ particles as crack healing agents in yttria stabilized zirconia thermal barrier coatings.* J. Eur. Ceram. Soc., 2015. **35**: p. 4507-4511.

8. Carabat, A.L., van der Zwaag, S., Sloof, W. G., *Creating a Protective Shell for Reactive MoSi2 Particles in High-Temperature Ceramics.* J. Am. Ceram. Soc., 2015. **98**: p. 2609–2616.

9. Raghavan, S., Wang, H., Porter, W. D., Dinwiddie, R. B., Mayo, M. J., *Thermal properties of zirconia co-doped with trivalent and pentavalent oxides.* Acta Materialia, 2001. **49**: p. 169–179.

10. Raghavan, S., Wang, H., Dinwiddie, R. B., Porter, W. D., Vassen, R., Stover, D., Mayo, M. J., *Ta2O5/Nb2O5 and Y2O3 Co-doped Zirconias for Thermal Barrier Coatings.* J. Am. Ceram. Soc., 2004. **87**: p. 431–437.

11. Shen, Y., Leckie, R. M., Levi, C. G., Clarke, D. R., *Low thermal conductivity without oxygen vacancies in equimolar YO1.5 + TaO2.5- and YbO1.5 + TaO2.5-stabilized tetragonal zirconia ceramics* Acta Materialia, 2010. **58**: p. 4424–4431.

12. Bose, S., Hecht, R. J., *Thermal properties of MoSi2 and SiC whisker-reinforced MoSi2.* Journal of Materials Science, 1992. **27**: p. 2749-2752.

13. Ramasesha, S.K., Tantri, S. P., Bhattacharya, A. K., *MoSi2 AND MoSi2 - Based materials as structural ceramics.* Metals Materials And Processes, 2000. **12**: p. 181 - 190.

14. Scardi, P., Leoni, M., Cernuschi, F., Figari, A., *Microstructure and Heat Transfer Phenomena in Ceramic Thermal Barrier Coatings.* J. Am. Ceram. Soc., 2001. **84**: p. 827–835.

15. Schlichting, K.W., Padture, N. P., Klemens, P. G., *Thermal conductivity of dense and porous yttria-stabilized zirconia.* Journal of Materials Science, 2001. **36**: p. 3003 – 3010.

16. Bjorneklett, A., Haukeland, L., Wigren, J., Kristiansen, H., *Effective medium theory and the thermal conductivity of plasma-sprayed ceramic coatings.* Journal of Materials Science, 1994. **29**: p. 4043-4050.

17. Nait-Ali, B., Haberko, K., Vesteghem, H., Absi, J., Smith, D. S., *Thermal conductivity of highly porous zirconia.* J. Eur. Ceram. Soc., 2006. **26**: p. 3567–3574.

18. Ponnusami, S.A., TurtelTaub, S., van der Zwaag, S., *Cohesive-zone modelling of crack nucleation and propagation in particulate composites.* Engineering Fracture Mechanics, 2015. **149**: p. 170-190.

19. www.sambaproject.eu. *Self-healing thermal barrier coatings for prolonged lifetime*. 2013 [cited 2016].

20. Kopp, H., *Investigations of the Specific Heat of Solid Bodies.* Phil. Trans. R. Soc. Lond., 1865. **155**: p. 71-202.

21. Barin, I., *Thermochemical data of pure substances*. 3rd ed. 1995, Germany: VCH GmbH, Weinhem.

22. Moreira, D.C., Sphaier, L. A., Reis, J. M. L., Nunes, L. C. S., *Experimental investigation of heat conduction in polyester–Al2O3 and polyester–CuO nanocomposites.* Experimental Thermal and Fluid Science, 2011. **35**: p. 1458-1462.

23. Progelhof, R.C., Throne, J. L., Ruetsch, R. R., *Methods for Predicting the Thermal Conductivity of Composite Systems: A Review.* Polym. Eng. Sci., 1976. **16**: p. 615-625.

24. Wemhoff, A.P., *Thermal conductivity predictions of composites containing percolated networks of uniform cylindrical inclusions.* Int. J. Heat Mass and Transfer, 2013. **62**: p. 255-262.

25. Stille, U., *Der Entmagnetisierungsfaktor und Entelektrisierungsfaktor fur Rotationsellipsoide.* Archiv fur Elektrotechnik, 1944. **38**: p. 91-101.

26. Cernuschi, F., Bison, P., Moscatelli, A., *Microstructural characterization of porous thermal barrier coatings by laser flash technique.* Acta Materialia, 2009. **57**: p. 3460–3471.

27. Cernuschi, F., Ahmaniemi, S., Vouristo, P., Mantyla, T., *Modelling of thermal conductivity of porous materials: application to thick thermal barrier coatings.* J. Eur. Ceram. Soc., 2004. **24**: p. 2657–2667.

28. Nielsen, L.E., *The Thermal and Electrical Conductivity of Two-Phase Systems.* Ind. Eng. Chem., Fundam., 1974. **13**: p. 17-20.

29. Nielsen, L.E., *Thermal Conductivity of Particulate-Filled Polymers.* J. Appl. Polym. Sci., 1973. **17**: p. 3819-3820.

30. Oya, T., Nomura, T., Tsubota, M., Okinaka, N., Akiyama, T., *Thermal conductivity enhancement of erythritol as PCM by using graphite and nickel particles.* App. Therm. Eng., 2013. **61**: p. 825-828.

31. Ren, L., Pashayi, K., Fard, H. R., Kotha, S. P., Borca-Tasciuc, T. and R. Ozisik, *Engineering the coefficient of thermal expansion and thermal conductivity of polymers filled with high aspect ratio silica nanofibers.* Composites: Part B, 2014. **58**: p. 228-234.

32. Wang, Z., Kulkarni, A., Deshpande, S., Nakamura, T., Herman, H., *Effects of pores and interfaces on effective properties of plasma sprayed zirconia coatings.* Acta Materialia, 2003. **51**: p. 5319-5334.

33. Hirano, T., Kaise, M., *Electrical resistivities of single‐crystalline transition‐metal disilicides.* J. Appl. Phys., 1990. **68**: p. 627-633.

34. Ito, K., Hayashi, T., Nakamura, N., *Electrical and thermal properties of single crystalline Mo5X3 (X=Si, B, C) and related transition metal 5-3 silicides.* Intermetallics, 2004. **12**: p. 443–450.

35. Yang, F., Zhao, X., Xiao, P., *Thermal conductivities of YSZ/Al2O3 composites.* J. Eur. Ceram. Soc., 2010. **30**: p. 3111-3116.

36. Schulz, B., *Thermal conductivity of porous and highly porous materials.* HTHP, 1981. **12**: p. 661-664.

37. Knudsen, M., *The kinetic theory of gases: some modern aspects.* 1950, London: Methuen & Company.
38. Lide, D.R., *CRC handbook of chemistry and physics*. 2004: CRC Press.

39. Stauffer, D., *Scaling Theory of Percolation Clusters.* Physics Letters, 1979. **54**: p. 1-74.

40. Stauffer, D., Aharony, A., *Introduction to Percolation Theory*. 1991, Taylor & Francis: Washington, DC.

41. Hatta, H., Taya, M., Kulacki, F. A., Harder, J. F., *Thermal Diffusivities of Composites with Various Types of Filler.* J. Compos. Mater., 1992. **26**: p. 612-625.

42. Kim, B.-W., Pfeifer, S., Park, S.-H., Bandaru, P. R., *The experimental determination of the onset of electrical and thermal conductivity percolation thresholds in carbon nanotube-polymer composites.* Mater. Res. Soc. Symp. Proc., 2011. **1312**: p. 281-286.

43. Lin, F., Bhatia, C. S., Ford, J. D., *Thermal Conductivities of Powder-Filled Epoxy Resins.* J. Appl. Polym. Sci., 1993. **49**: p. 1901-1908.

44. Pfeifer, S., Park,S.-H., Bandaru, P. R., *Analysis of electrical percolation thresholds in carbon nanotube networks using the Weibull probability distribution.* J. Appl. Phys., 2010. **108**: p. 024305-1-024305-4.

45. Sundstrom, D.W., Lee, Y.-D., *Thermal Conductivity of Polymers Filled with Particulate Solids.* J. Appl. Polym. Sci., 1972. **16**: p. 3159-3167.

46. Pal, R., *On the Lewis–Nielsen model for thermal/electrical conductivity of composites.* Composites: Part A, 2008. **39**: p. 718–726.

47. Weber, E.H., Clingerman, M. L., King, J. A., *Thermally Conductive Nylon 6,6 and Polycarbonate Based Resins. II. Modeling.* J. Appl. Polym. Sci., 2003. **88**: p. 123-130.

List of Figure Captions:

Figure 1: The process of converting a SEM image into FE mesh and calculating the effective thermal conductivity according to the calculated temperature field. A sample with 20 vol. % $MoSi_2$ was used as an example. Notice that no elements have been generated for the pores.

Figure 2: Thermal conductivity of $MoSi_2$ as a function of temperature [11].

Figure 3: SEM images of the specimen surfaces for pure YSZ matrix (a), YSZ and 10 vol. % $MoSi_2$ (b) and YSZ with 20 vol. % $MoSi_2$ (c).

Figure 4: XRD peak positions collected from SPS samples. Peaks have been assigned to different phases found from the analysis.

Figure 5: Thermal diffusivity of the YSZ/$MoSi_2$ as a function of temperature.

Figure 6: Thermal conductivity of the YSZ/$MoSi_2$ as a function of temperature calculated using Eq. 1.

Figure 7: Comparison of the temperature dependent thermal conductivity based on FE and the Bruggeman model solution for composite samples with 10 vol. % (a) and 20 vol. % $MoSi_2$ filler (b). Dashed lines show lower and upper boundary regions for asymmetric Bruggeman model.

Figure 8: Thermal conductivity of composites consisting of $MoSi_2$ spheres in YSZ matrix. Solid line is theoretical predictions using Eq. 3-6. Blues dots show experimental values measured at room temperature for the actual volume fraction of $MoSi_2$ particles, as stated in Table 1.

Figure 9: Thermal conductivity of composites consisting of $MoSi_2$ spheres in YSZ matrix. Dots show experimental data fitted into Nielsen model (solid line) according to the actual volume fraction of $MoSi_2$ particles [26].

Figure 10: Conductivity of Ar as a function of pore sizes at various temperatures according to Eq. 10.

Figure 11: Effective thermal conductivity values as a function of the $MoSi_2$ aspect ratio *a:c* calculated for modelled artificial microstructures.

Figure 12: Heat fluxes inside the ceramic composites with different $MoSi_2$ shapes: real microstructure, k_{eff} = 4.18 $Wm^{-1}K^{-1}$ (a-b); a:c = 1:1, k_{eff} = 3.38 $Wm^{-1}K^{-1}$ (c-d); a:c = 32:1, k_{eff} = 7.77 $Wm^{-1}K^{-1}$ (e-f) and a:c = 1:32, k_{eff} = 2.75 $Wm^{-1}K^{-1}$ (g-h). The shape of $MoSi_2$ strongly affects the heat fluxes as they serve as channels for thermal flow.

Table 1: Characteristics of SPS samples used for thermal diffusivity measurements.

$MoSi_2$ volume %	Porosity %	Measured volume % of $MoSi_2$	Density (g cm^{-3})
0	11.84±1.3	0	5.49
10	7.96±3.0	13.5±4.4	5.53
20	10.72±1.4	21.8±1.5	5.84

*Corresponding author: justyna.kulczyk-malecka@manchester.ac.uk
Tel: +441613063590

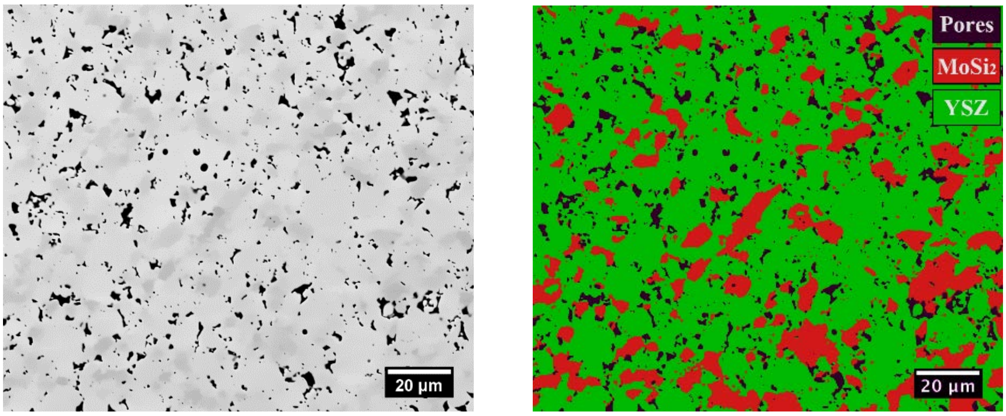

(a) Filtered SEM image

(b) Phase map

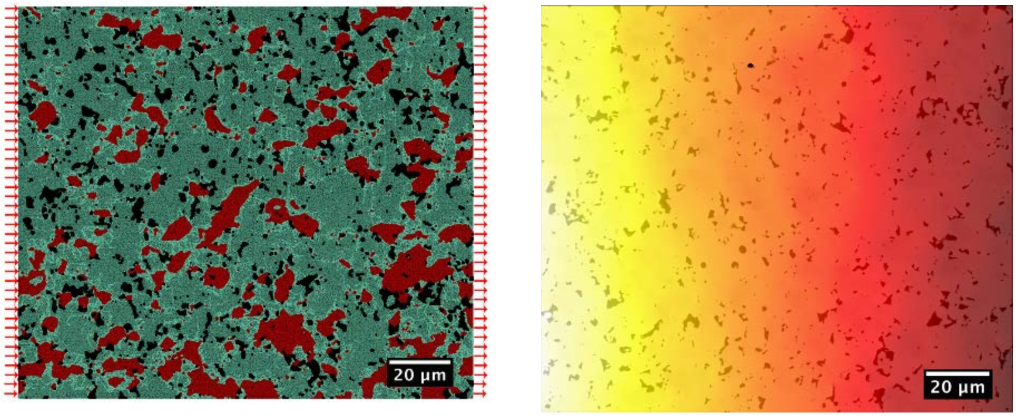

(c) FE Mesh

(e) Temperature Field

Figure 1

*Corresponding author: justyna.kulczyk-malecka@manchester.ac.uk
Tel: +441613063590

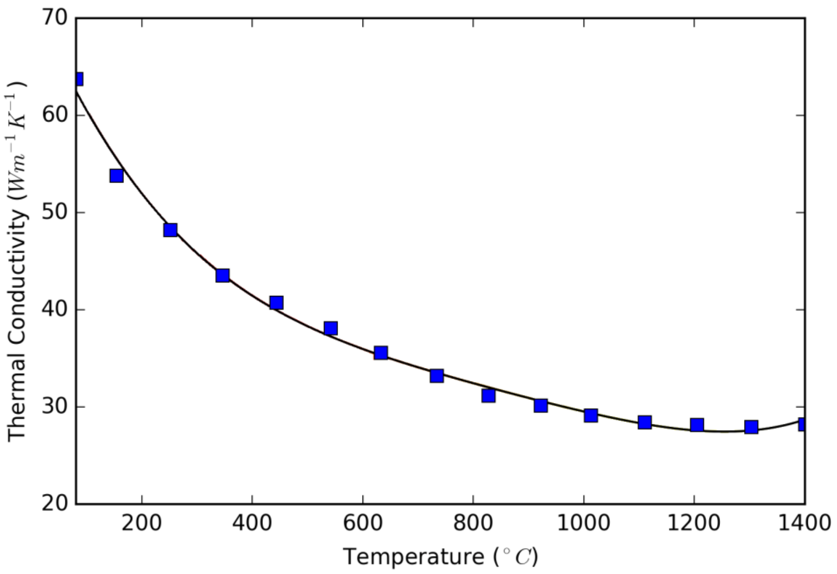

Figure 2

*Corresponding author: justyna.kulczyk-malecka@manchester.ac.uk
Tel: +441613063590

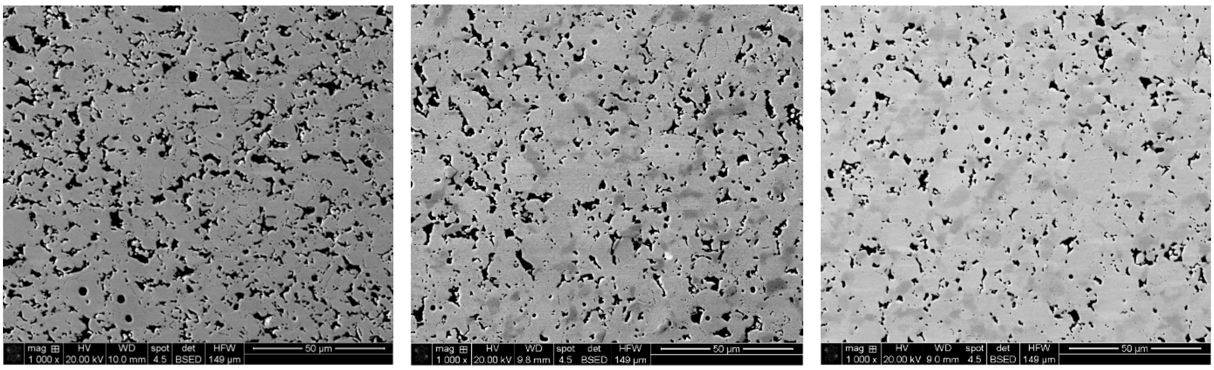

(a) (b) (c)

Figure 3

*Corresponding author: justyna.kulczyk-malecka@manchester.ac.uk
Tel: +441613063590

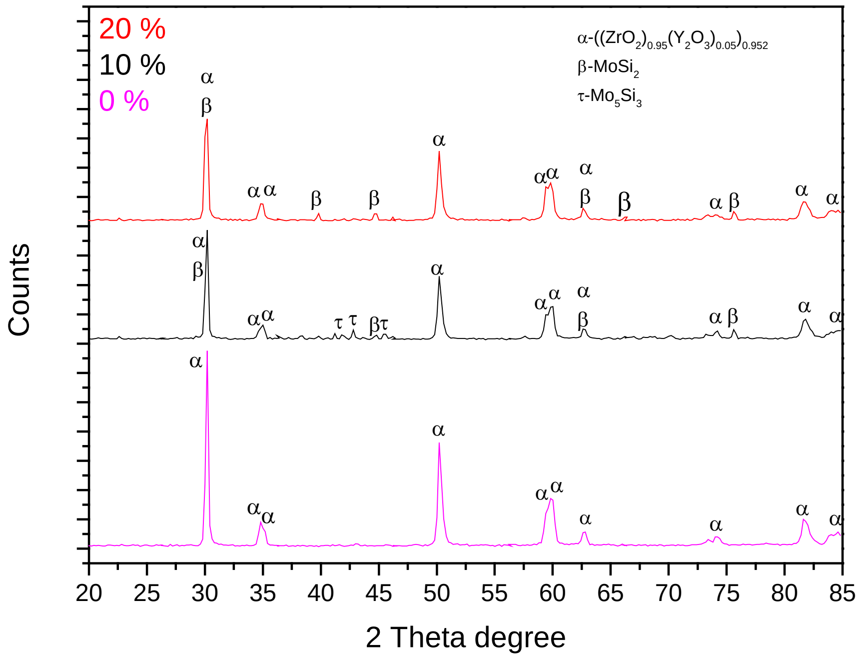

Figure 4

*Corresponding author: justyna.kulczyk-malecka@manchester.ac.uk
Tel: +441613063590

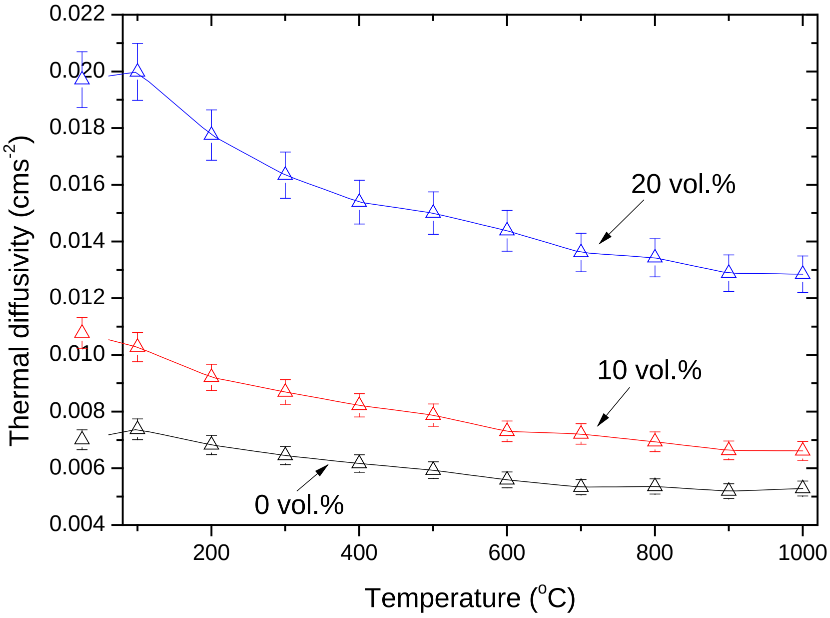

Figure 5

*Corresponding author: justyna.kulczyk-malecka@manchester.ac.uk
Tel: +441613063590

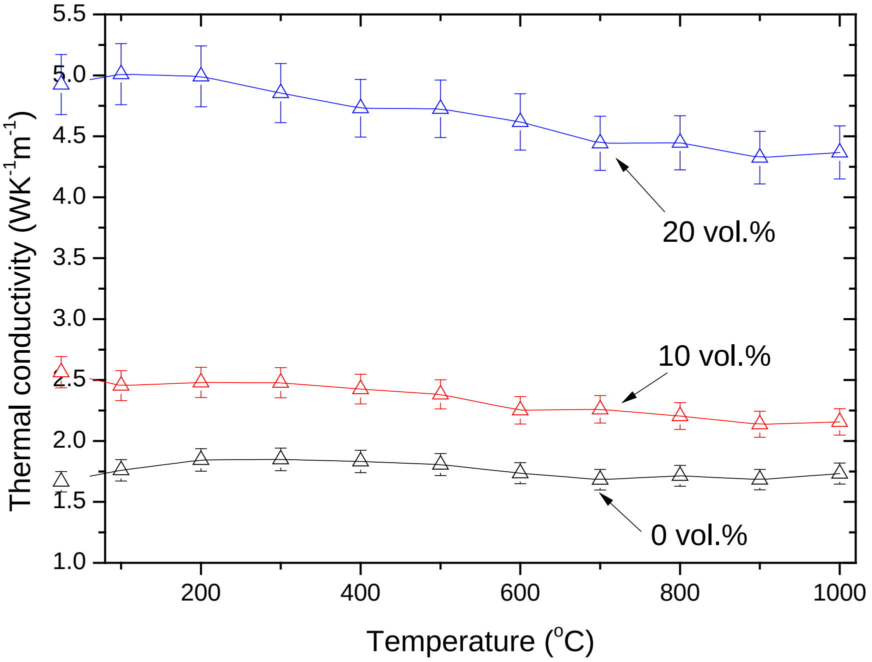

Figure 6

*Corresponding author: justyna.kulczyk-malecka@manchester.ac.uk
Tel: +441613063590

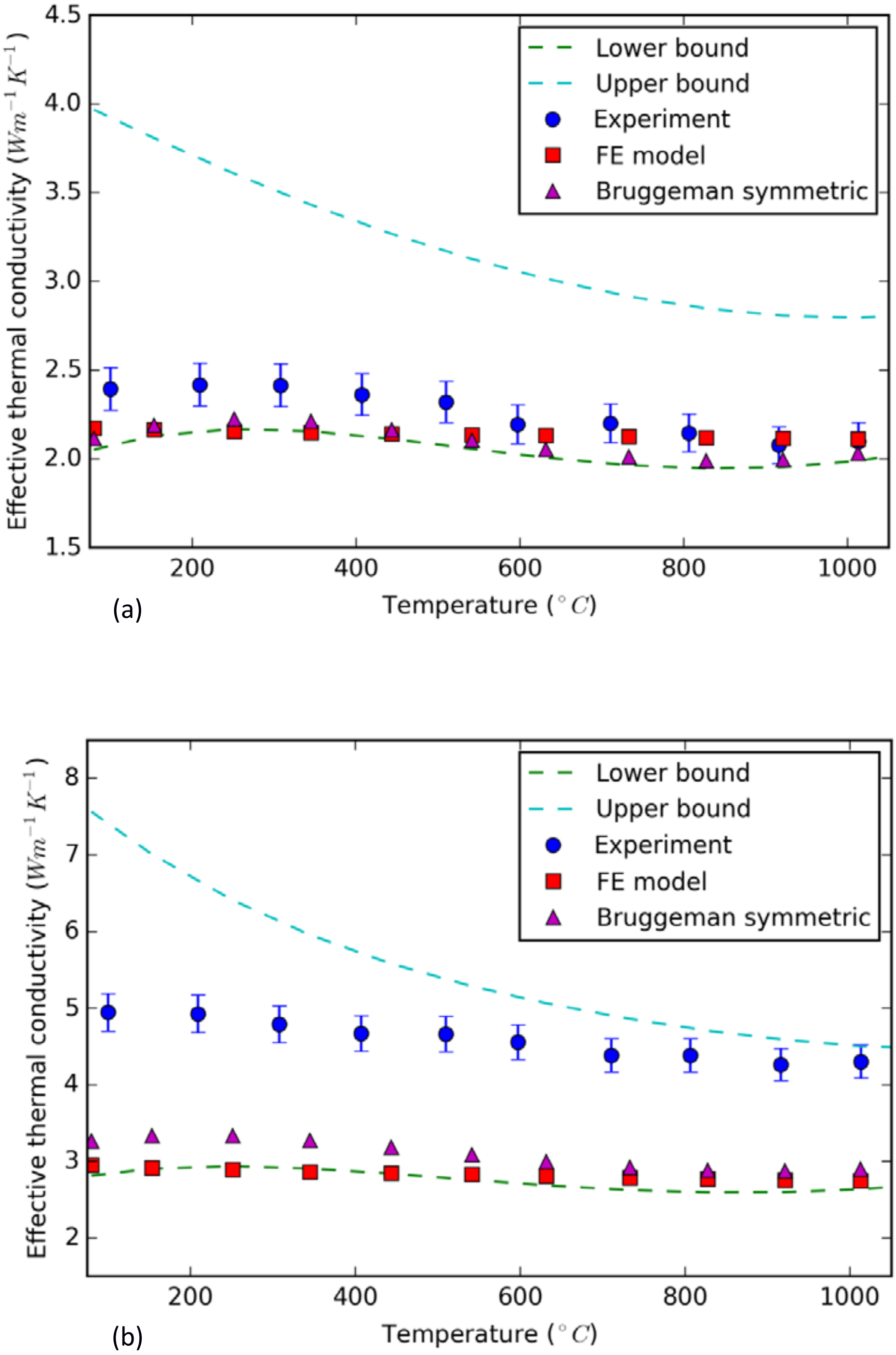

(a)

(b)

Figure 7

*Corresponding author: justyna.kulczyk-malecka@manchester.ac.uk
Tel: +441613063590

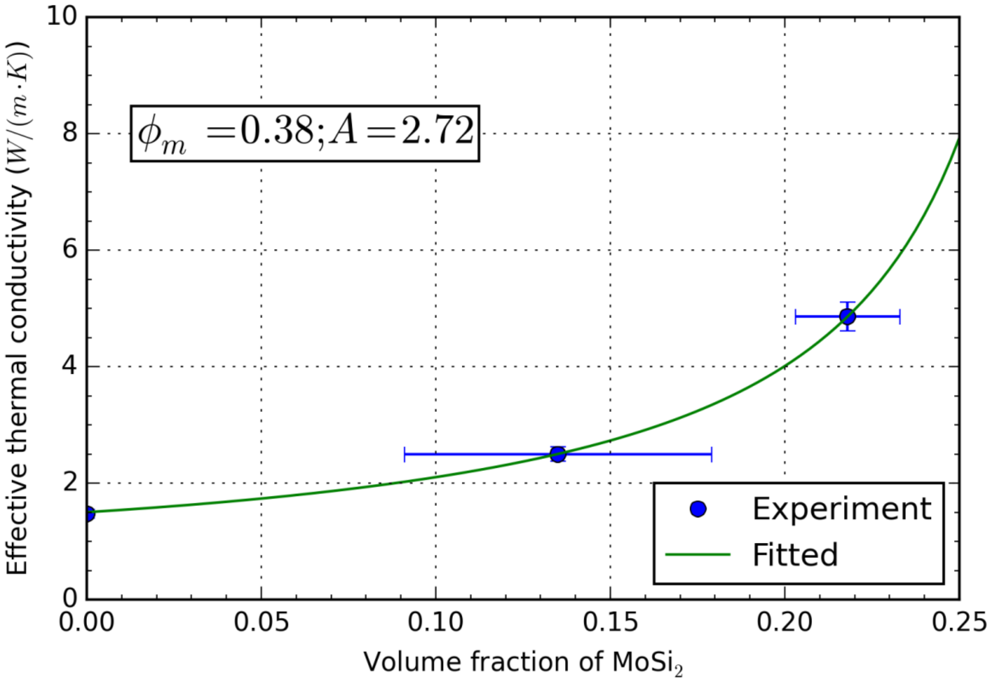

Figure 8

*Corresponding author: justyna.kulczyk-malecka@manchester.ac.uk
Tel: +441613063590

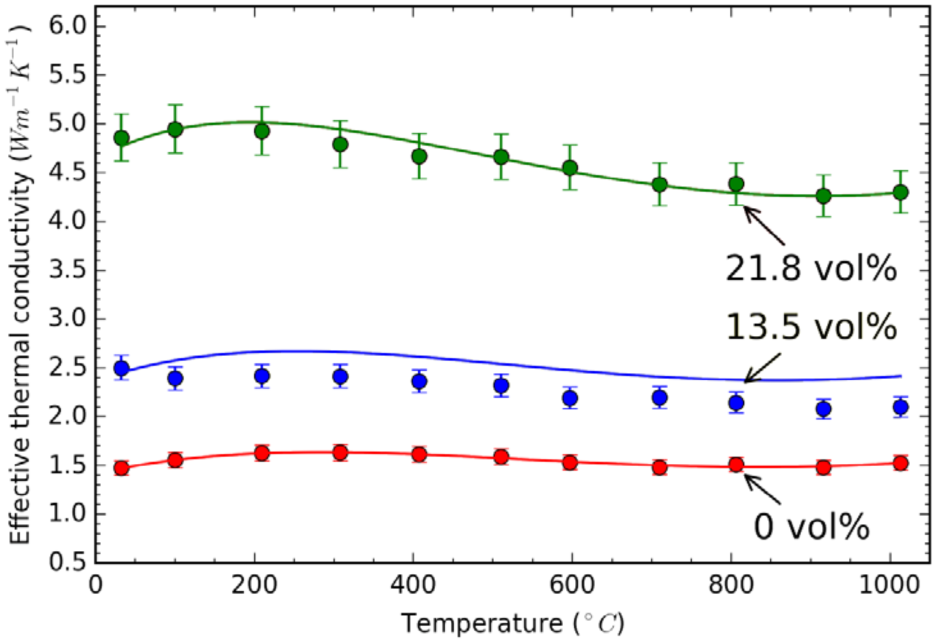
Effective thermal conductivity ($Wm^{-1}K^{-1}$)
6.0
5.5
5.0
4.5
4.0
3.5
3.0
2.5
2.0
1.5
1.0
0.5
0
200
400
600
800
1000
Temperature ($^\circ C$)
21.8 vol%
13.5 vol%
0 vol%

Figure 9

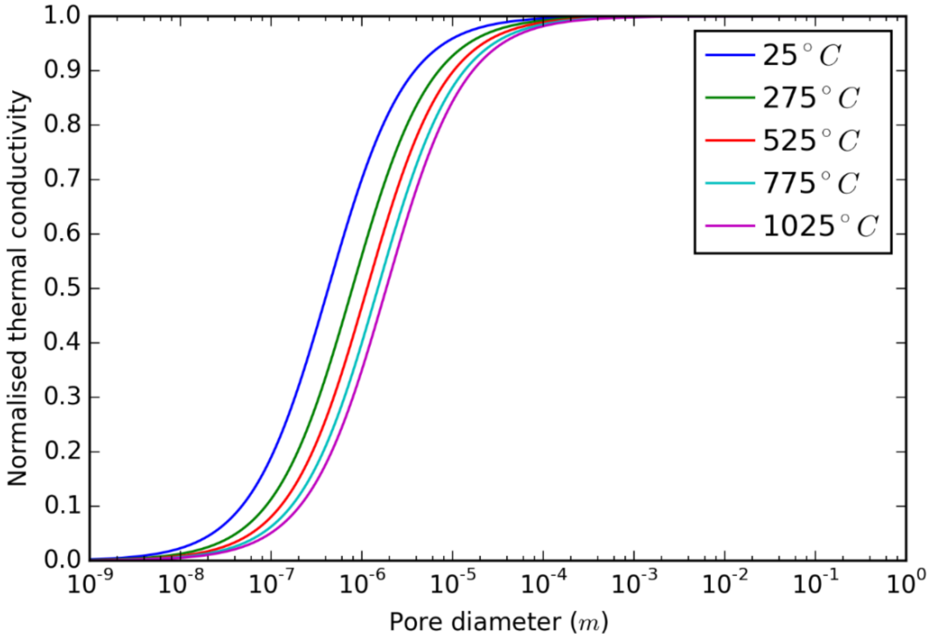

Figure 10

*Corresponding author: justyna.kulczyk-malecka@manchester.ac.uk
Tel: +441613063590

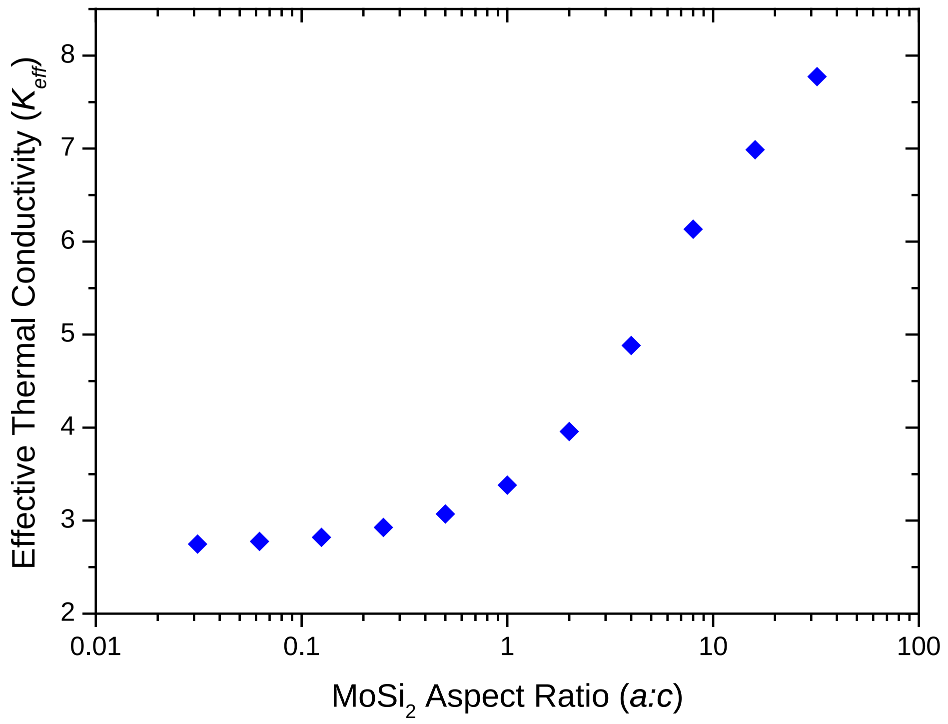

Figure 11

*Corresponding author: justyna.kulczyk-malecka@manchester.ac.uk
Tel: +441613063590

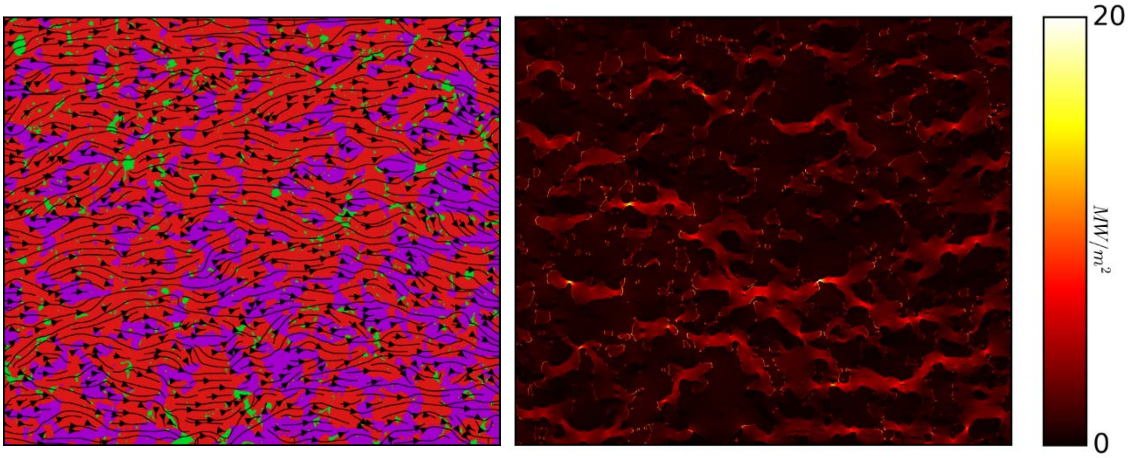

(a) Flux Vector (b) Magnitude Map

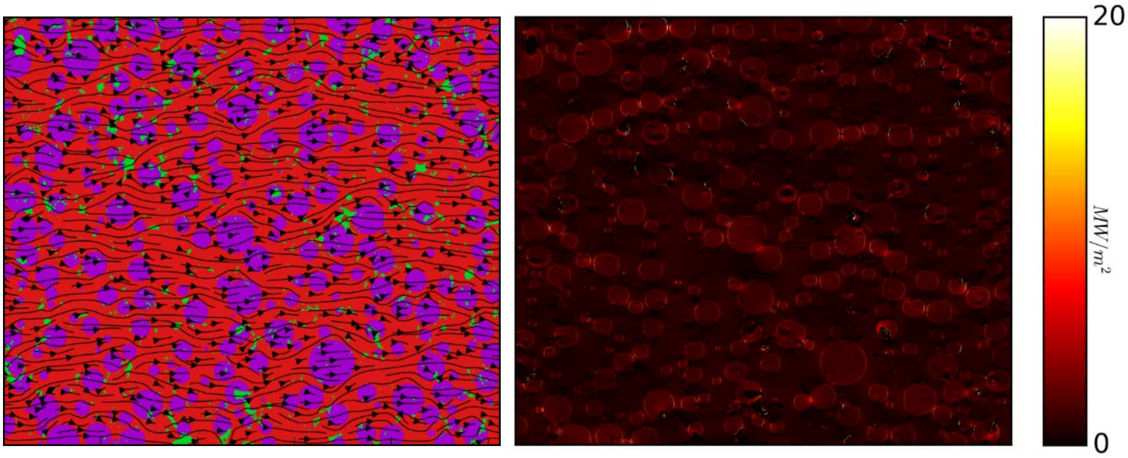

(c) Flux Vector (d) Magnitude Map

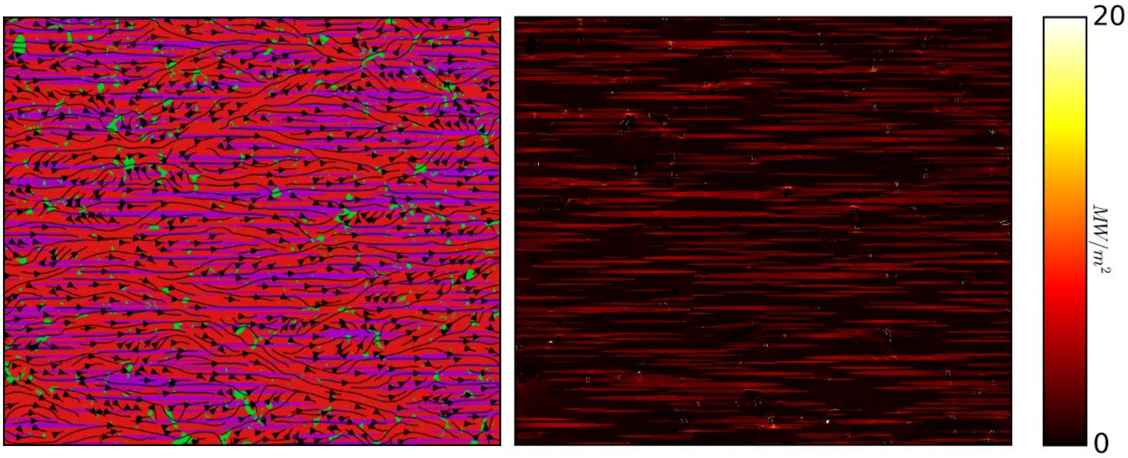

(e) Flux Vector (f) Magnitude Map

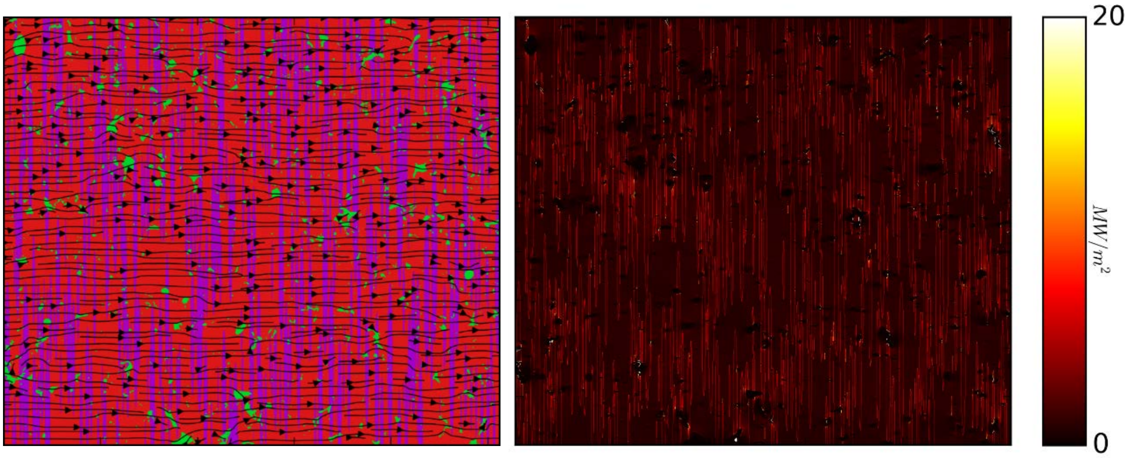

(g) Flux Vector

(h) Magnitude Map

Figure 12

*Corresponding author: justyna.kulczyk-malecka@manchester.ac.uk
Tel: +441613063590